metals

MDPI

Article

Mechanical Fracture of Aluminium Alloy (AA 2024-T4), Used in the Manufacture of a Bioproducts Plant

Luis Fabian Urrego [1], Olimpo García-Beltrán [2], Nelson Arzola [3] and Oscar Araque [1,*]

[1] Departamento de Desarrollo Tecnológico, Facultad de Ingeniería, Universidad de Ibagué, Ibagué 730002, Colombia; 2120151024@estudiantesunibague.edu.co
[2] Facultad de Ciencias Naturales y Matemáticas, Universidad de Ibagué, Carrera 22 Calle 67, Ibagué 730002, Colombia; jose.garcia@unibague.edu.co
[3] Research Group in Multidisciplinary Optimal Design, Departamento de Ingeniería Mecánica y Mecatrónica, Universidad Nacional de Colombia, Bogotá 111321, Colombia; narzola@unal.edu.co
* Correspondence: oscar.araque@unibague.edu.co

Abstract: Aluminium alloy (AA2024-T4) is a material commonly used in the aerospace industry, where it forms part of the fuselage of aircraft and spacecraft thanks to its good machinability and strength/weight ratio. These characteristics allowed it to be applied in the construction of the structure of a pilot plant to produce biological extracts and nano-encapsulated bioproducts for the phytosanitary control of diseases associated with microorganisms in crops of *Theobroma cacao* L. (Cacao). The mechanical design of the bolted support joints for this structure implies knowing the performance under fatigue conditions of the AA2024-T4 material since the use of bolts entails the placement of circular stress concentrators in the AA2024-T4 sheet. The geometric correction constant (Y) is a dimensionless numerical scalar used to correct the stress intensity factor (SIF) at the crack tip during propagation. This factor allows the stress concentration to be modified as a function of the specimen dimensions. In this work, four compact tension specimens were modeled in AA2024-T4, and each one was modified by introducing a second circular stress concentrator varying its size between 15 mm, 20 mm, 25 mm, and 30 mm, respectively. Applying a cyclic load of 1000N, a load ratio R=-1 and a computational model with tetrahedral elements, it was determined that the highest SIF corresponds to the specimen with a 30 mm concentrator with a value close to 460 MPa.mm$^{0.5}$. Where the crack propagation had a maximum length of 53 mm. Using these simulation data, it was possible to process each one and obtain a mathematical model that calculates the geometric correction constant (Y). The calculated data using the new model was shown to have a direct relationship with the behavior obtained from the simulation.

Keywords: crack; fatigue; geometric factor; support vector regression; pilot plant

check for updates

Citation: Urrego, L.F.; García-Beltrán, O.; Arzola, N.; Araque, O. Mechanical Fracture of Aluminium Alloy (AA 2024-T4), Used in the Manufacture of a Bioproducts Plant. *Metals* **2023**, *13*, 1134. https://doi.org/10.3390/met13061134

Academic Editors: Haitao Cui and Qinan Han

Received: 9 May 2023
Revised: 10 June 2023
Accepted: 13 June 2023
Published: 16 June 2023

1. Introduction

Theobroma cacao (Cocoa) is considered one of the most important raw materials in international trade; it is a source of foreign exchange in 58 producing countries, highlighting that 89% of this production is found in Ivory Coast, Ghana, Indonesia, Nigeria, Brazil, Ecuador, Malaysia and Cameroon [1]. Cocoa production is sometimes affected by environmental, physical, and chemical factors and inadequate pest and disease control [2]. This crop is mainly infected by disease-causing microorganisms, among which *Moniliophthora roreri* and *Phytophthora* spp. stand out, which are the two main risk factors that directly affect annual cocoa production [3,4]. This is why management alternatives for these diseases, such as the use of plant extracts and essential oils (EO), should be sought, being favorable for environmental sustainability and human health [5]. This implies the development of an infrastructure capable of producing the raw material used in the production of bio-based products.

The study of the phenomenon of fracture has its origin in work proposed by Griffith (1921, 1924); the researcher Irwin (1957) made an important advance by proposing the analysis of fracture toughness as a function of stress, the toughness of a material is obtained from the applied stress and the crack length, but given the different test configurations, these values are known as a function of the failure modes called Stress Intensity Factor (SIF) K_I (Opening), K_{II} (in-plane shear) and K_{III} (out-of-plane shear). Estimation of the SIF in materials with linear elastic behavior (LEFM) is possible by quantifying the nominal stress and crack size. The use of the finite element method (FEM) allows testing for various configurations due to the versatility of the method; using the SMART component integrated into the latest versions of ANSYS finite element software, it is possible to perform simulations to verify the behavior of the geometric factor accompanying the determination of the SIF in the different failure modes.

Researchers have worked on this method, Nairn [6] has proposed the analysis of the geometric factor as a correction factor of the general SIF equation and that it can be expressed as a function of crack length (a) and width (W), on the other hand, for the author Mecholsky, the geometric factor (Y) for semi-elliptical cracks in materials of high hardness and brittleness is used to explain the position and shape of the crack because it is a function of an angle (θ) between the surface of the crack front and any peripheral point above it [7], otherwise, authors Taylor, Cornetti and Pugno, cataloged this geometric factor not only in terms of geometry but also in terms of the crack notch [8], on the other hand, when analyzing fatigue crack propagation, the geometrical factor is included in an expression known as the initial value of propagation for short cracks (a_0), which according to the authors B. Atzori, P. Lazzarin and G. Meneghetti, occurs at the point of intersection between the change in realized stress ($\Delta\sigma$) and the different values of toughness (ΔK), where the geometrical factor is calculated using a simulation in ANSYS 5.6 software [9].

The authors Smith and Scattergood have analyzed ceramic materials defining toughness as a sum of two different toughnesses: (K_{bend}), which is defined as a toughness that is a function of the stress intensity factor and the residual toughness ($K_{residual}$) that results from the residual stress field due to strain, an equation is obtained to determine the value of the toughness (K_{bend}) by an exponential equation, which involves a shape factor and the crack depth [10]. However, when analyzing materials with a higher degree of ductility, the empirical approaches of authors J.C. Newman and I.S. Raju obtained an equally accepted behavior for the determination of toughness [11].

On the other hand, when testing chromium steels, authors Nix and Lindley determined that the behavior of the shape factor (C_s) was also exponential in nature, where the basis again was the ratio (a/c), where (a) is the crack depth, and (c) is the crack length, where the values of this ratio were previously calculated by subjecting chromium steel specimens On the other hand, when testing chromium steels, the authors Nix and Lindley established that the behavior of the form factor, identifying that for the tests developed, the fracture toughness equation must involve a factor called (M_f), which is a crack front correction factor [12].

These correction factors have been the product of a rigorous algebraic analysis, where the basis of each of the equations that describe these factors, part of the simulations in finite element programs, which provide the input values necessary to apply the respective analysis algorithms, as proposed by the authors Clarke, Griebsch and Simpson, who explain how it is possible to glimpse different situations of mechanical nature by means of the Support Vector Regression (SVR), algorithm, this algorithm allows from some input values in the Cartesian plane, to obtain an equation that adjusts to the distribution of given values, considering the dispersion (ξ) of the same one, and the margin (ε) between the support vectors [13]. This algorithm uses the principles of Lagrangian optimization, simultaneously involving Kernel functions, which can have a polynomial, Gaussian or Sigmoidal nature, and as explained by researchers Schölkopf and Smola [14], authors Heydari and Choupani, indicate a correction factor for fracture toughness of a logarithmic nature based on the rate of energy release [15], authors El-Desouky and El-Wazery, indicated fracture toughness for materials with a high degree of brittleness, using a fifth-degree polynomial (F_1), whose variable is the relation (a/W), where (a) is the crack length and (W) is the length of the cross-sectional area [16].

The models for the geometric factor for compact specimens that are currently planned in the literature are based on specimens that have a single stress concentrator.

Aluminum alloys are widely used in industry to reduce the weight of structural components in machine design. Their light weight, easy machinability and excellent fatigue strength make these alloys ideal materials for manufacturing in the modern world. One of the most recent applications is in the high-speed rail industry, where 5083P-O Aluminium alloy is involved in the design of train bodies, leading to increased running speed and improved assembly performance [17].

The goal of the present work is to evaluate the behavior of this parameter when there are two stress concentrators arranged in the specimen geometry since it has been visually observed that the crack rupture direction is affected by the size and location of the concentrator with respect to the propagation plane. In the same way, the study of the geometrical factor implies a study of the stress intensity factor at the crack tip, which means that this last parameter must also be analyzed for the geometrical conditions proposed. The main differentiating feature lies in determining the stress intensity factor by applying the FEM method and then processing this data by means of the SVR algorithm. Applied to non-standardized specimens with variable diameter stress concentrators. Allowing the data obtained by the simulation to be used within the Nadaraya–Watson estimator to find a mathematical model that explains the behavior under variable tensile loading and crack propagation.

The importance of the model to be developed consists in its use as an element for joining bolted joints in structures with diameter variation with the purpose of establishing life projection parameters useful for design processes.

2. Materials and Methods

2.1. Material and Specimens

In this article, a modified compact tension specimen (MCTE) was used based on the ASTM-E399 standard, where the value of W was set at 100 mm and its thickness at 10 mm. In the same way, a stop hole of variable diameter was set in; in the same way, a stop hole of variable diameter was fixed in 4 different specimens; therefore, 4 simulations were performed for each modified compact specimen. The dimensions are shown in Figure 1. For the configuration of the SMART method used in ANSYS, it was necessary to characterize the Aluminium alloy (AA 2024-T4). This is hardened by a thermal aging process and presents the mechanical properties contained in [18] and presented in Table 1; similarly, the author Zyad Nawaf Haji [19] characterized the fatigue deformation parameters for AA2024-T4. These parameters are determined from the Ramberg–Osgood and Coffin–Mason equations that describe well the cyclic behavior of the material, but they are not physical laws [20]. These parameters are presented in Table 2.

Table 1. Mechanical properties AA2024-T4 [18].

Property	Value
Density (Kg/m^3)	2770
Coefficient of thermal expansion (1/C)	0.000023
Young's Modulus (MPa)	71,000
Poisson's Ratio	0.33
Shear Modulus (MPa)	26,692
Bulk Modulus (MPa)	69,608

The mechanical and fatigue properties of the AA2024-T4 used for the ANSYS simulation are shown below.

The authors B.M. Faisal, A.T. Abass and A.F. Hammadi [21] subjected to fatigue tests several specimens of AA2024-T4, determining its characteristic S-N curve, which is presented in Figure 2. Table 3 shows the values for the C and m constants for AA2024-T4 determined by authors Yang Guang, Gao Zengliang, Xu Feng and Wang Xiaogui [22] by subjecting eleven specimens to fatigue tests.

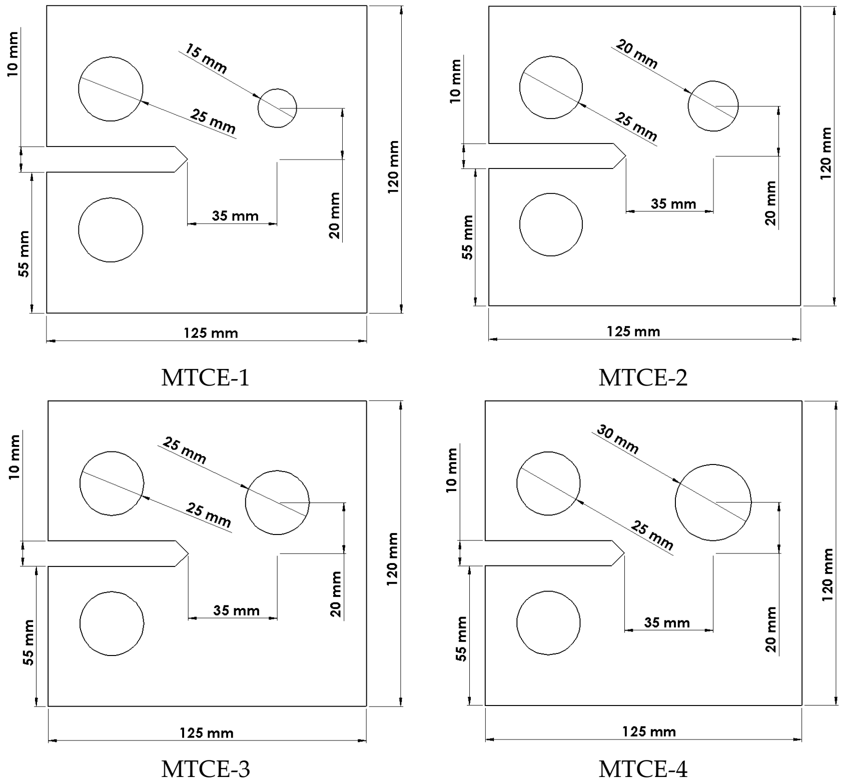

Figure 1. Dimensions of modified compact specimens used.

Table 2. Fatigue Parameters AA2024-T4 [20].

Parameter	Value
Strength Coefficient (MPa)	714
Strength Exponent	−0.078
Ductility Coefficient	0.166
Ductility Exponent	−0.538
Cyclic Strength Coefficient (MPa)	502
Cyclic Strain Hardening Coefficient	0.15

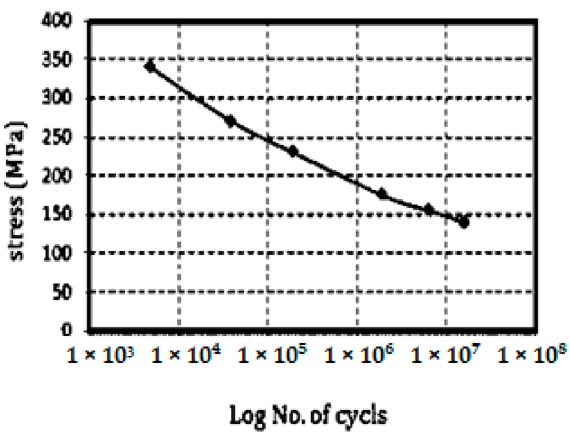

Figure 2. Characteristic fatigue behavior of the material AA 2024-T4 [21].

Table 3. Paris' Law Constants [22].

Constant	Value
C	5.75×10^{-8}
m	3.09

All modified compact tension specimens were subjected to failure mode 1 (opening), which causes a unidirectional cyclic stress perpendicular to the crack plane; using a force of 1000 N, using a Stress Ratio (R) = -1, since according to author C.M. Hudson fatigue cracks in Aluminium alloy AA 2024 propagate at a faster rate with $R = -1$ than with $R = 0$ when the same load was applied in both tests. Apparently, the compression portion of the loading cycle accelerates crack growth in this material [23]. Therefore, we proceeded to perform the simulation using ANSYS Mechanical ADPL 21R1, from which we calculated the K_I values and the crack extension values (a) in each sub-step of the solution. It was taken from Equation (1), formulated by R.P. Wei [24] for high-strength aluminum subjected to cyclic axial loading.

$$\Delta K_{I\ max} = Y \Delta\sigma \sqrt{\pi a} \tag{1}$$

Expressing ΔK_I as $(K_{I\ max} - K_{I\ min})$ and $\Delta\sigma$ as $(\sigma_{max} - \sigma_{min})$, it is possible to derive Equation (2) algebraically.

$$K_{I\ max} = Y \sigma_{max} (1 - R) \sqrt{\pi a} \tag{2}$$

Subtracting for Y gives:

$$Y = \frac{K_{I\ max}}{\sigma_{max}(1 - R)\sqrt{\pi a}} \tag{3}$$

Which is a dimensional expression that, for the purposes of the investigation, will be compared with the relative crack length, which is expressed by a ratio a/W and is also dimensionless.

2.2. Computational Model Using SMART Method

To achieve a better analysis of the SIF at the crack tip, the meshing was defined using a Patch Conforming Method defined by Tetrahedral elements, these elements, according to the ANSYS usage guide [25], are unique to the SMART method. Tetrahedral elements are 3-dimensional in nature, have a quadratic displacement behavior and are well suited for modeling irregular meshes. The element is defined by 10 nodes that have 3 degrees of freedom in each of the x, y, and z nodal directions see Figure 3.

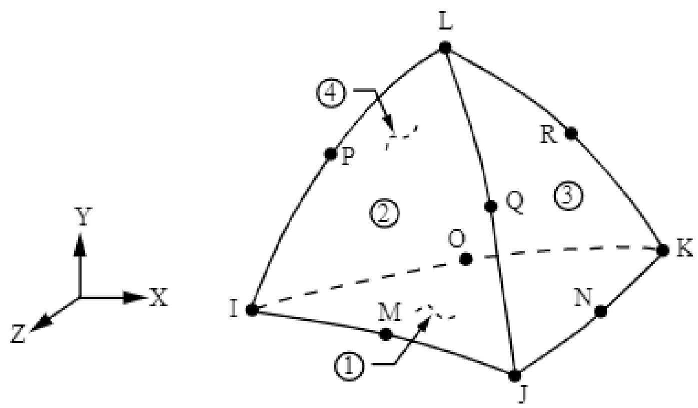

Figure 3. Tetrahedral elements.

The element has plasticity, hyperelasticity, creep, tensile stiffness, good deflection, and tension capabilities. It also has mixed formulation capabilities to simulate deformations of nearly incompressible elastoplastic materials and fully incompressible hyperelastic materials [26]. Similarly, the Refinement method was used to perform sectorized refinements in the crack front and its adjacent areas, as well as in the areas surrounding the circular stress concentrators (stop holes). The grids, the number of elements and nodes of each computational model used are shown below.

The Smart Crack Growth component used in the current research does not require the placement of a pre-crack geometry; however, it does require the involvement of 3 parameters defined within the Fracture-Premesh Crack block that are defined based on the geometry of the notch placed in the specimen. These parameters must be nodal surfaces adjacent to the crack front. The first is defined as a function of the nodes located on the edge of the crack front, which in the present work, we call the front, and interprets the place at which the crack propagation would start; the second, which we call the top, interprets the nodes located on the upper adjacent surface to the crack front; the third, which we call the bottom, interprets the nodes located on the lower adjacent part of the crack front.

Similarly, Figure 4a illustrates the nodes on the crack front (front), Figure 4b illustrates the nodes on the top surface adjacent to the crack front (top), Figure 4c illustrates the nodes on the bottom surface adjacent to the crack front (bottom) and Figure 4d illustrates the location of the pre-crack conditions with the coordinate axes, inferring that the propagation will be along the x-axis.

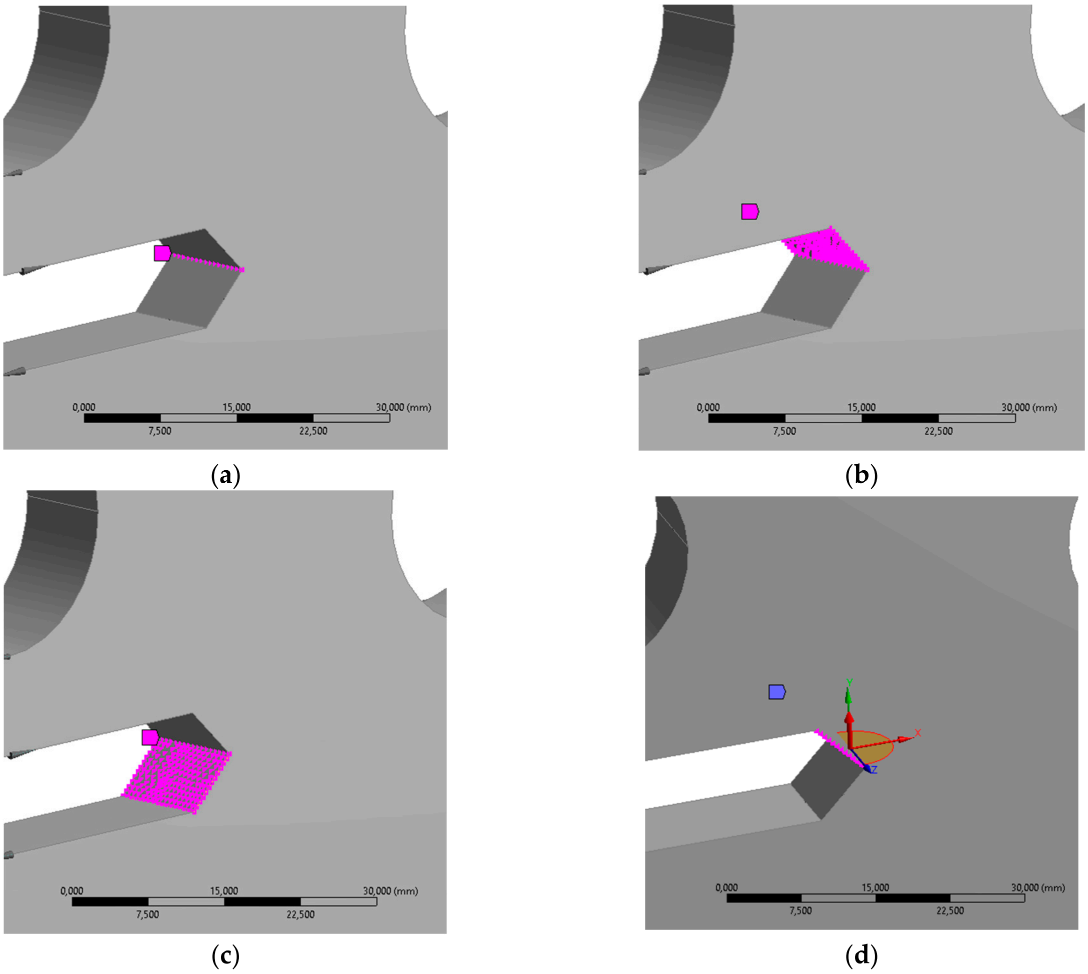

Figure 4. (**a**) illustrates the nodes on the crack front (front), (**b**) illustrates the nodes on the top surface adjacent to the crack front (top), (**c**) illustrates the nodes on the bottom surface adjacent to the crack front (bottom) and (**d**) illustrates the location of the pre-crack conditions with the coordinate axes, inferring that the propagation will be along the x-axis.

In Figures 5–8, the working specimen is presented, showing the number of elements and nodes for each of the variations in the size of the diameter of the stress concentrator elements.

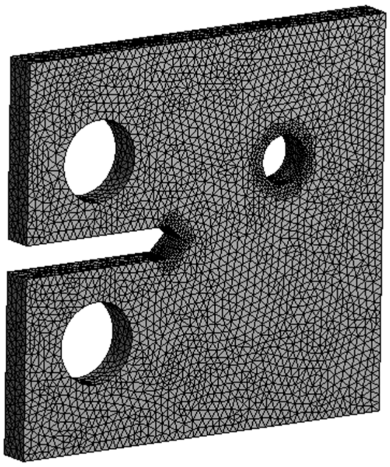

Figure 5. MTCE-1 mesh with 101742 elements and 151424 nodes.

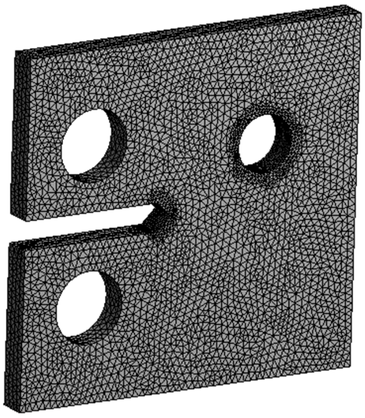

Figure 6. MTCE-2 Mesh with 104899 elements and 156293 nodes.

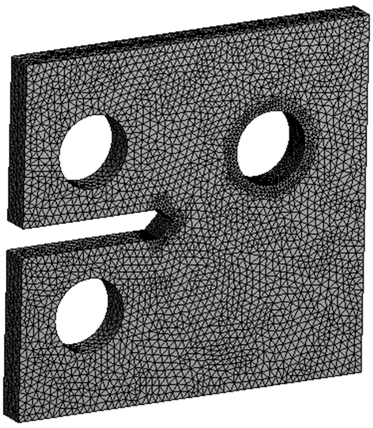

Figure 7. MTCE-3 Mesh with 107059 elements and 159635 nodes.

The numerical model was defined using the patch-forming method with tetrahedral elements. A general refinement was applied to the entire geometry of each specimen by setting the size of each element to 2.5 mm, and then a surface refinement was applied to each of the concentrators. Within the analysis setup, a time-defined solution was established with 10 s as the time limit and 0.5 s as the time in each solution step.

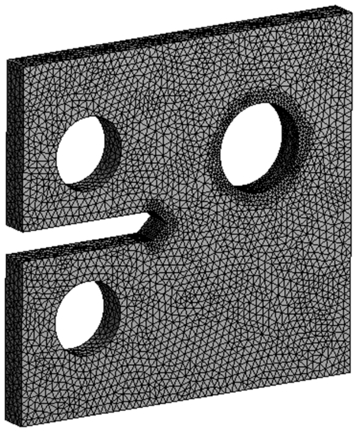

Figure 8. MTCE-4 Mesh with 99726 elements and 149780 nodes.

2.3. Data Processing Using Support Vector Regression (SVR) and Nadaraya-Watson Estimator (NWE)

The SVR algorithm is an algorithm for linear or non-linear regression of points in the Cartesian plane, whose purpose is to find the equation of the hyper-plane that interpolates all the points, based on the use of Kernel functions $K(x)$ (see Table 4). Furthermore, considering the margin between vectors (ε), the dispersion that exists between the margins and the points furthest from it (ζ) and the arithmetic mean of the data (μ). These are variables that can be imposed during regressions in this way. The quality of the regressions performed can be measured in terms of the coefficient of determination (R^2), since the closer this value is to 1, the higher the quality of the regression. The rationale of the SVR algorithm lies in the quadratic optimization of a Gram matrix, which is maximized subject to a real domain condition to find the Lagrange multipliers [26].

Table 4. Kernel Equations.

Kernel Equations	
Linear	$K(\vec{X}_n, \vec{X}'_n) = \vec{X}_n^{\,T} \cdot \vec{X}'_n$
Polynomial	$K(\vec{X}_n, \vec{X}'_n) = \left(\vec{X}_n \cdot \vec{X}'_n\right)^d$
Gaussian	$K(\vec{X}_n, \vec{X}'_n) = e^{-\frac{\lVert \vec{X}_n - \vec{X}'_n \rVert^2}{2\sigma^2}}$
Sigmoidal	$K(\vec{X}_n, \vec{X}'_n) = \tanh\left(\left(\vec{X}_n \cdot \vec{X}'_n\right) + \varphi\right)$
Epanechnikov	$K(\vec{X}_n, \vec{X}'_n) = \frac{3}{4}\left(1 - \left(\vec{X}_n \cdot \vec{X}'_n\right)^2\right)$

The calculation of the weight values w_n that are calculated by means of the Lagrange multipliers were obtained by means of a code in Python language and from which the approximation was carried out by means of the Nadaraya-Watson estimator. To determine which of the Kernel equations shows similar behavior.

According to author Larroca, F., the Nadaraya–Watson estimator is a type of non-parametric estimator that uses an equation, $\hat{m}(x)$, and a fit parameter, ε_o, to interpolate a series of data in the Cartesian plane, this equation, $\hat{m}(x)$, is given as a function of a weighted average of a Kernel density equation (see Table 4), which is assigned to each of the points taken [27]. However, the author Cai. Z. [28] proposes that the function $\hat{m}(x)$ is altered with weight values, w_n, to improve its fit, therefore, its general form is given by:

$$Y_{pred} = \hat{m}(x) \pm \varepsilon_o \quad (4)$$

According to the authors Demir, S. and Toktamis, O. [29], the use of the Kernel within ENW implies changing the dot product between vectors by the expression $\frac{x_n - x}{h}$, then, the function $\hat{m}(x)$ is posed as:

$$\hat{m}(x) = \frac{\sum_{i=1}^{n} w_n \cdot K\left(\frac{x_n - x}{h}\right) y_n}{\sum_{i=1}^{n} w_n \cdot K\left(\frac{x_n - x}{h}\right)} \tag{5}$$

According to the author Fan, J., K symbolizes a Kernel density equation, x_n is the x-axis coordinate of each point in the Cartesian plane, y_n is the y-axis coordinate of each point in the Cartesian plane, n is the number of points in the plane, and h is a parameter known as Bandwidth that controls the accuracy of the interpolating equation with respect to the Cartesian plane data; this last parameter is considered optimal when the highest accuracy is obtained, that is, the smallest mean square error (MSE). This error is calculated as [30].

$$MSE = \frac{1}{n}\left(Y_{pred} - y_n\right)^2 \tag{6}$$

Then, the equation interpolating the values is expressed as follows:

$$Y_{pred} = \frac{\sum_{i=1}^{n} w_n \cdot K\left(\frac{x_n - x}{h}\right) y_n}{\sum_{i=1}^{n} w_n \cdot K\left(\frac{x_n - x}{h}\right)} \pm \varepsilon_o \tag{7}$$

The analysis procedure used to process the data obtained by using the finite element method is illustrated in Figure 9, where it is shown that the desired Kernel equation and the data obtained from the simulation are used to complete the Gram matrix. This same data will then be used in the NWE to multiply the vector weights obtained from the Lagrangian optimization problem. From this multiplication, a mathematical model is finally obtained. It should be noted that the definition of the dependent and independent variables is maintained from the beginning of the processing and does not change at the end of the processing.

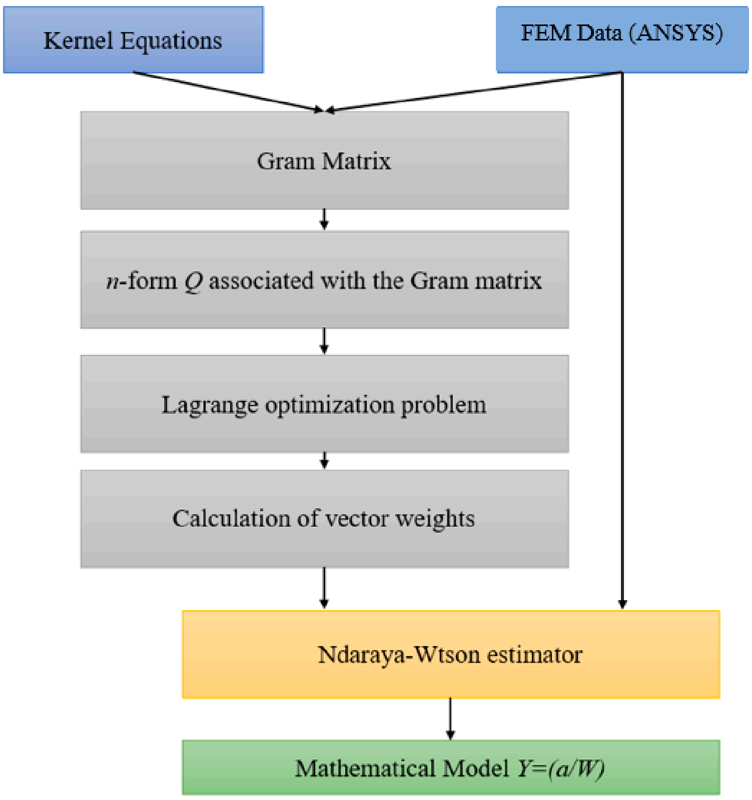

Figure 9. Methodology of analysis applied to FEM data.

3. Results

Figure 10 illustrates the behavior of the SIF in failure mode I with respect to crack length (a):

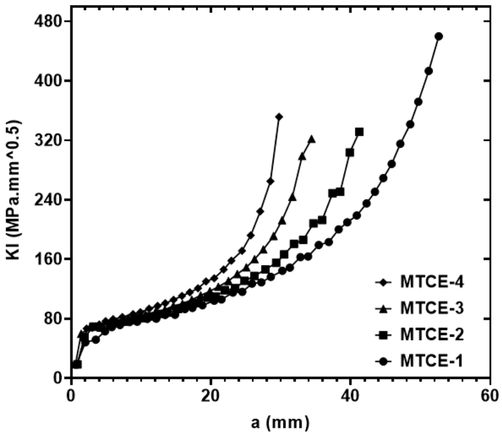

Figure 10. Mode I SIF with respect to crack length (a) for each specimen tested.

Based on the results illustrated in Figure 11, it is observed that MTCE-1 does not present a failure in the concentrator as observed in the other specimens. Therefore, the propagation length was higher in this specimen; this can be explained by the function of a greater cross-sectional area existing in MTCE-1 since the diameter of its circular concentrator is 15 mm, which is the smallest among the other specimens; Figure 11 shows the crack propagation obtained in each specimen.

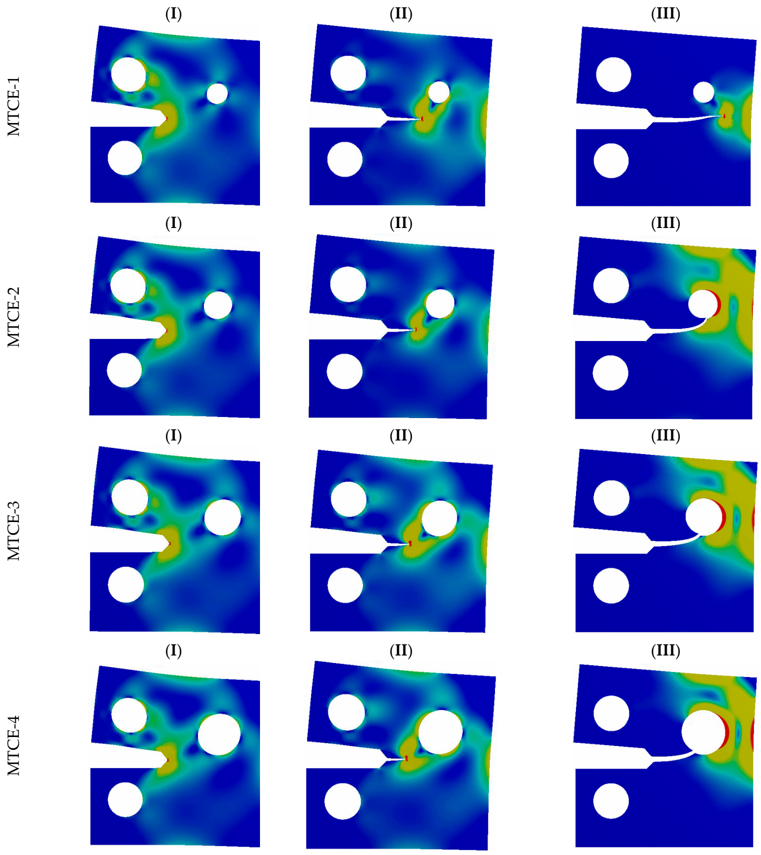

Figure 11. Crack propagation obtained in each specimen, (**I**) illustrates the solution in the first sub-step of the solution, (**II**) illustrates the propagation in the middle sub-step of the solution and (**III**) illustrates the propagation in the last sub-step of the solution.

Figure 12 shows the behavior of the geometric correction factor $(\boldsymbol{Y})$ as a function of the relative crack length $(\boldsymbol{a}/\boldsymbol{W})$.

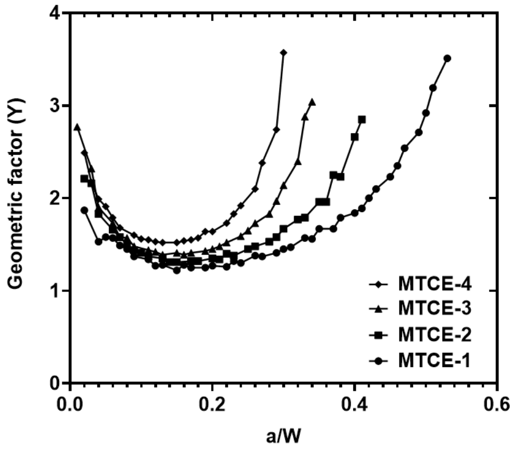

Figure 12. Geometric factor compared to the relative crack length.

From these calculated data, a regression was developed by applying the concepts of the SVR and the Nadaraya-Watson estimator (NWE), applying the Epanechnikov Kernel since, according to the authors Chu, C. Y., Henderson, D. J., and Parmeter, C. F, this is the equation that shows the highest efficiency when interpolating data placed in a Cartesian plane [30].

This model was found using a value for Bandwidth (h) equal to 0.47 and a value for ε_o of 0.4, whose associated curve is illustrated in Figure 13.

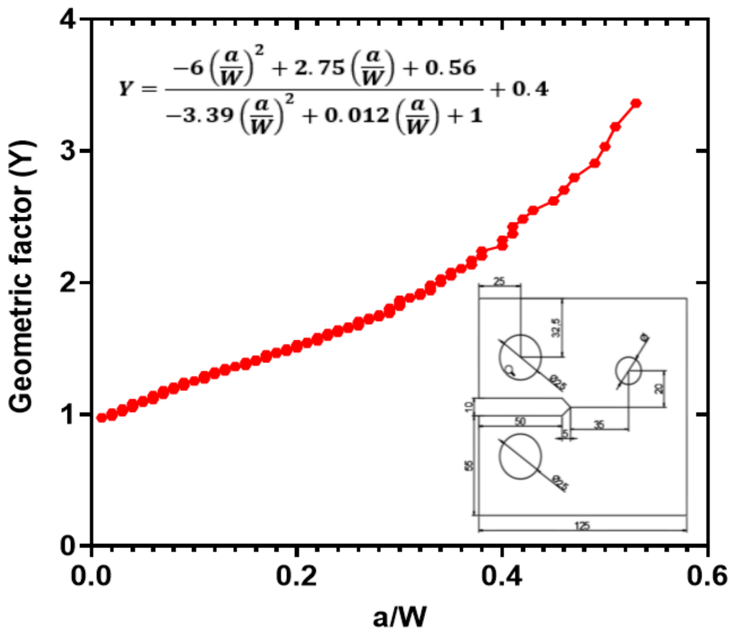

Figure 13. Mathematical model relating the geometric correction factor as a function of relative crack length.

This model has an MSE of 11.2%, which may be due to the high dispersion presented when $0.2 \leq a/W \leq 0.4$ as from this value, in Figure 12. A high dispersion of the data is observed; this dispersion is caused by the variation in the diameter of the circular stress concentrator used in each MTCE analyzed, so it is prudent to infer that when the specimens analyzed present unique geometric characteristics, the mathematical models obtained must be similarly unique for each MTCE, since for the specimens that are standardized, there are already validated models for their geometries.

4. Discussion

With the model found in Figure 13, the design of a bolted joint can be proposed from Equation (2), where the hole through which the bolt will pass is assumed to be a circular stress concentrator whose diameter is among those used in each of the MTCE specimens. Then. Starting from Equation (2), we have that:

$$K_{I\ max} = Y\sigma_{max}(1-R)\sqrt{\pi a} \tag{8}$$

By subtracting for σ_{max}, the expression is left as:

$$\sigma_{max} = \frac{K_{I\ max}}{Y(1-R)\sqrt{\pi a}} \tag{9}$$

Figure 14a illustrates one of the 10 mm diameter holes used in the assembly of the pilot plant structure, and Figure 14b illustrates the force direction (black) in the hole due to the estimated weight of the equipment. The load value used is 1000 N, corresponding to the force exerted on the joint under cyclic loading with R = −1.

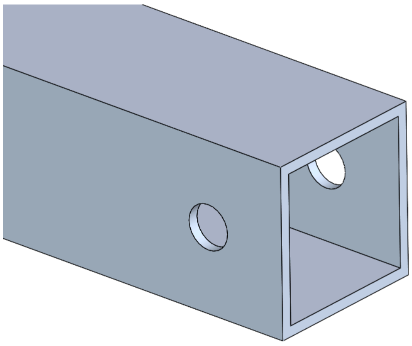

(**a**)

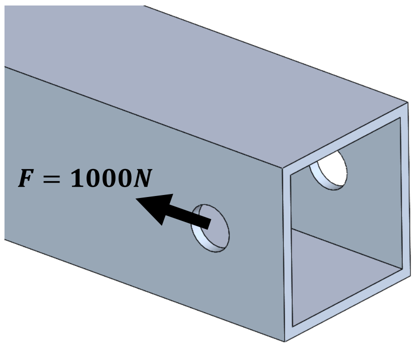

(**b**)

Figure 14. (**a**) support bolt hole, (**b**) forces assumed for joint design.

Assuming that the material of the structure will be AA-2024-T4, then the joint dimensions can be calculated by the following expression:

$$A = \frac{(\tau_{Al})\left(\frac{-6\left(\frac{a}{w}\right)^2+2.75\left(\frac{a}{W}\right)+0.56}{-3.39\left(\frac{a}{W}\right)^2+0.012\left(\frac{a}{W}\right)+1}+0.4\right)(1-R)\sqrt{\pi a}}{K_{Imax}} \tag{10}$$

By performing the calculations using Equation (10), we obtain that the fatigue resistance area of the joint should not be less than 76.2 MPa. Figure 15 illustrates a rendering of the structure model designed.

It is observed that both the behavior of the SIF and the crack length (a) found in this research have a similarity with the data found by the authors Alshoaibi, Abdulnaser M. [31], in this study, the behavior of crack propagation is analyzed in aluminum alloy 7075-T6 specimens, which were subjected to a force of 20 KN and a stress ratio of 0.1, finding crack lengths of almost 30 mm, and with values for the SIF of about 7000 KPa.mm$^{0.5}$.

The reason for the difference between this study and the current one lies firstly in the composition of each of the alloys, the 7075-T6 alloy being stronger, and secondly, the high magnitude of the applied force with respect to the force proposed in the present investigation, which was 1KN, however, the behavior of the SIF is like that found in this article. Figure 16 illustrates a comparison of the graphs of SIF vs. crack length (a) between the works of the authors Alshoaibi, Abdulnaser M. (a) and the present one (b).

Figure 15. Model of the designed structure.

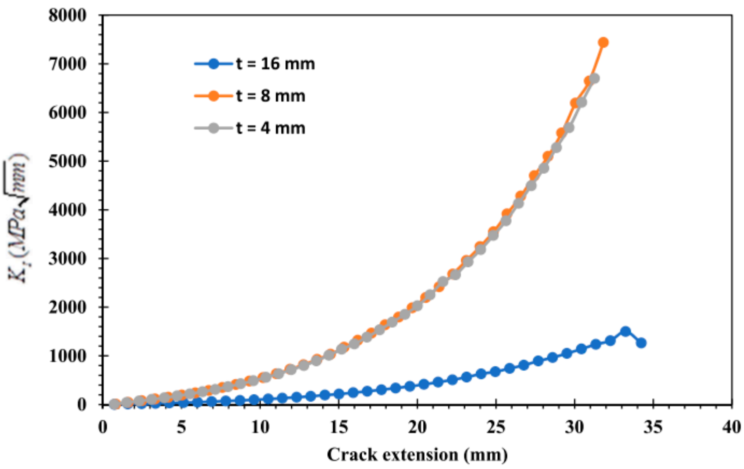

(a)

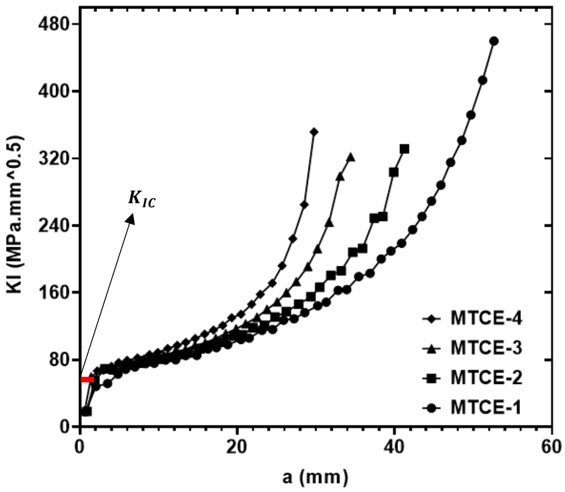

(b)

Figure 16. SIF data comparison. (**a**) Illustrates a comparison of the graphs of SIF vs. crack length between the works of the authors Alshoaibi, Abdulnaser M. and (**b**) the present one.

Looking at the scale of the values obtained in Figure 16. It is possible to compare them with the results found by the authors J. M. D. Rahmatabadi, M. Pahlavani, A. Bayati and R. Hashemi [32], who, in their work, propose the use of a standardized compact stress specimen with a size between 23.75 mm × 22.8 mm using a dual phase melt at 770 °C of Mg LZ71 and Mg LZ91 alloys subjected to quasi-static loading which varied between 0 N and 900N. In the results, the authors show that for a load of around 900 N a $K_{IC} = 18.9$ MPa·m$^{1/2}$ is generated. If we look at Figure 16, we have that for all the studied MTCEs, the approximate K_{IC} value is 70 MPa·mm$^{1/2}$, which dimensionally equals 2.21 MPa·m$^{1/2}$. This clear difference between the K_{IC} values could be explained by the thickness of the plates used, being the thinner plate used by the authors J. M. D. Rahmatabadi, M. Pahlavani, A. Bayati and R. Hashemi, which is 1.7 mm thicker than the one with the smallest stress cross-sectional area, while the one used in this work is 10 mm thick, which implies that much less stress will be concentrated on the 10 mm plate.

5. Conclusions

Computational models were generated for each proposed MTCE using a high density of elements in the meshes, with an average of 103356 elements. Likewise, the use of sectored refinements in the notch and in the circular stress concentrator facilitated the analysis of each of the models. Observing the behavior of the SIF in each MTCE, it can be deduced analytically that the presence of a circular stress concentrator alters the area where the stress applied to the specimen affects and therefore alters the SIF. This coincides with the behavior observed in Figure 9 since the presence of a smaller diameter concentrator implies a larger area of incidence of the cyclic stress; therefore, if there is a larger area of incidence, the stress along the cross-sectional area is smaller, and therefore, the SIF takes longer to reach high values, which results in a longer propagation length. When determining the geometric factor Y, it was observed that it increases as the diameter of the circular stress concentrator also increases; this is closely related to the behavior of the SIF since this factor was determined based on the data obtained from the SIF in failure mode I. The mathematical model found presented an MSE of 11.2%, fitting the geometric factor (Y) with a function that depends on the relative crack length (a/W).

From the propagation instants in Figure 10, it can be observed that the direction in which the crack propagates changes as the concentrator hole becomes larger. Based on this idea, it can be deduced that as the radius of the hole is farther away from the crack front plane, the propagation angle tends to maintain values close to 0°, while if the distance between the hole radius and the midline of the specimen becomes shorter, the propagation angles tend to be much higher.

It would be important to analyze the behavior of the propagation angle direction under the same geometrical conditions of the specimens shown in the present work, as well as to establish a relationship between the size of the second concentrator and the crack propagation direction.

The behavior of the crack propagation direction is determined by the crack length. If it is observed in Figure 10 (III) for each of the specimens, the propagation angle with respect to a horizontal axis becomes tighter as the crack length tends to be smaller. This behavior could be explained as a function of the reduction of the cross-sectional area because of the diameter change in the second circular concentrator.

The joint designed using Equation (10) for the bioplant structure proved to be useful at the time of construction since the structure will be subjected to vibration, which produces alternating stresses that fall on the bolted joint. The nomenclature used in the manuscript is shown in Table 5.

Table 5. Nomenclature.

Nomenclature		Greek Symbols	
K_I	Stress Intensity Factor Mode I	π	Pi number
a	Crack length	σ	Axial stress
W	Length measured from the point of grip to the end	ε_o	ENW Setting Parameter
a/W	Relative crack length	ε	Amplitude between support vectors
Y	Geometric correction factor	ζ	External margin between support vectors
h	Bandwidth	μ	Arithmetic mean of data
R	Stress ratio	**Subscripts**	
$K(x)$	Kernel Equation	NWE	Nadaraya–Watson Estimator
C	Paris law material constant	MTCE	Modified Tension Compact specimen
m	Paris law material constant	SIF	Stress Intensity Factor
$\hat{m}(x)$	Nadaraya—Watson equation	SVR	Support Vector Regression
w_n	Weight value of each vector	MSE	Mean Square Error

Author Contributions: Conceptualization, L.F.U., O.G.-B., N.A. and O.A.; Formal analysis, L.F.U., O.G.-B., N.A. and O.A.; Investigation, O.G.-B., N.A. and O.A.; Methodology, L.F.U., O.G.-B., N.A., and O.A.; Resources, O.G.-B. and O.A.; Writing—original draft, L.F.U.; Writing—review&editing, O.G.-B., N.A. and O.A. All authors have read and agreed to the published version of the manuscript.

Funding: The authors would like to thank the funding provided for this research from the Department of Research of the University of Ibagué, the Ministry of Science, Technology and Innovation, the Ministry of Education, the Ministry of Industry, Commerce and Tourism, and ICETEX, Program Ecosistema Científico-Colombia Científica, from the Francisco José de Caldas Fund, Grand RCFP44842-212-20184.

Institutional Review Board Statement: Not applicable.

Informed Consent Statement: Not applicable.

Data Availability Statement: Not applicable.

Acknowledgments: The authors would like to thank the University of Ibague research department, the funding provided for this research from the Ministry of Science, Technology and Innovation, the Ministry of Education, the Ministry of Industry, Commerce and Tourism, and ICETEX, Program Ecosistema Científico-Colombia Científica, from the Francisco José de Caldas Fund, Grand RCFP44842-212-20184.

Conflicts of Interest: The authors declare that they have no known competing financial interests or personal relationships that could have appeared to influence the work reported in this paper.

References

1. Sanchez-Capa, M.; Viteri-Sanchez, S.; Burbano-Cachiguango, A. New Characteristics in the Fermentation Process of Cocoa (*Theobroma cacao* L.) 'Super Á rbol' in La Joya de los. *Sustainability* **2022**, *14*, 7564. [CrossRef]
2. Gómez, E.H.; Campo, I.; Rosario, E.; Tapachula, K.C. Factores socieconómicos y parasitológicos que limitan la producción del cacao en Chiapas, México Socioeconomic and parasitological factors that limits cocoa production in Chiapas, Mexico, 2015. *Rev. Mex. Fitopatol.* **2015**, *33*, 232–246.
3. Chitiva-Chitiva, L.C.; Ladino-Vargas, C.; Cuca-Suárez, L.E.; Prieto-Rodríguez, J.A.; Patiño-Ladino, O.J. Antifungal Activity of Chemical Constituents from Phytopathogen Fungi of Cocoa. *Molecules* **2021**, *26*, 3256. [CrossRef] [PubMed]
4. Guerrini, A.; Sacchetti, G.; Rossi, D.; Paganetto, G.; Muzzoli, M.; Andreotti, E.; Tognolini, M.; Maldonado, M.E.; Bruni, R. Bioactivities of *Piper aduncum* L. and *Piper obliquum* Ruiz & Pavon (Piperaceae) essential oils from Eastern Ecuador. *Environ. Toxicol. Pharmacol.* **2009**, *27*, 39–48. [CrossRef]
5. Guerrero, R.; Risco, G.; Cevallos, O.; Villamar, R.; Peñaherrera, S. Extractos vegetales: Una alternativa para el control de enfermedades en el cultivo de cacao (*Theobroma cacao*). *Ing. Innovación* **2020**, *8*, 2326. [CrossRef]

6. Nairn, J.A. Direct comparison of anisotropic damage mechanics to fracture mechanics of explicit cracks. *Eng. Fract. Mech.* **2018**, *203*, 197–207. [CrossRef]
7. Mecholsky, J.J. Fracture mechanics principles. *Dent. Mater.* **1995**, *11*, 111–112. [CrossRef]
8. Taylor, D.; Cornetti, P.; Pugno, N. The fracture mechanics of finite crack extension. *Eng. Fract. Mech.* **2005**, *72*, 1021–1038. [CrossRef]
9. Atzori, B.; Lazzarin, P.; Meneghetti, G. Fracture mechanics and notch sensitivity. *Fatigue Fract. Eng. Mater. Struct.* **2003**, *26*, 257–267. [CrossRef]
10. Smith, S.M.; Scattergood, R.O. Crack-Shape Effects for Indentation Fracture Toughness Measurements. *J. Am. Ceram. Soc.* **1992**, *75*, 305–315. [CrossRef]
11. Newman, J.C., Jr.; Raju, I. An empirical stress-intensity factor equation for the surface crack. *Eng. Fract. Mech.* **1981**, *15*, 185–192. [CrossRef]
12. Nix, K.J.; Lindley, T.C. The Application of Fracture Mechanics to Fretting Fatigue. *Fatigue Fract. Eng. Mater. Struct.* **1985**, *8*, 143–160. [CrossRef]
13. Clarke, S.M.; Griebsch, J.H.; Simpson, T.W. Analysis of Support Vector Regression for Approximation of Complex Engineering Analyses. *J. Mech. Des.* **2004**, *127*, 1077–1087. [CrossRef]
14. Smola, A.J.; Scholkopf, B. A tutorial on support vector regression. *Stat. Comput.* **2004**, *14*, 199–222. Available online: http://citeseerx.ist.psu.edu/viewdoc/download;jsessionid=1CAD92EF8CCE726A305D8A41F873EEFC?doi=10.1.1.114.4288&rep=rep1&type=pdf%0Ahttp://download.springer.com/static/pdf/493/art%3A10.1023%2FB%3ASTCO.0000035301.49549.88.pdf?auth66=1408162706_8a28764ed0fae9 (accessed on 10 April 2023). [CrossRef]
15. Heydari, M.H.; Choupani, N. A New Comparative Method to Evaluate the Fracture Properties of Laminated Composite. *Int. J. Eng.* **2014**, *27*, 991–1004. [CrossRef]
16. El-Desouky, A.R. Mixed Mode Crack Propagation of Zirconia/Nickel Functionally Graded Materials. *Int. J. Eng.* **2013**, *26*, 885–894. [CrossRef]
17. Guo, K.; Gou, G.; Lv, H.; Shan, M. Jointing of CFRP/5083 Aluminum Alloy by Induction Brazing: Processing, Connecting Mechanism, and Fatigue Performance. *Coatings* **2022**, *12*, 1559. [CrossRef]
18. USA Department of Defense. *MIL-HDBK-2097, Military Handbook: Acquisition of Support Equipment and Associated Integrated Logistics Support*; USA Department of Defense: Washington, DC, USA, 1997.
19. Haji, Z. Low cycle fatigue behavior of aluminum alloys AA2024-T6 and AA7020-T6. *Diyala J. Eng. Sci.* **2010**, 127–137.
20. Meggiolaro, M. Statistical evaluation of strain-life fatigue crack initiation predictions. *Int. J. Fatigue* **2004**, *26*, 463–476. [CrossRef]
21. Faisal, B.M.; Abass, A.T.; Hammadi, A.F. Fatigue Life Estimation of Aluminum Alloy 2024-T4 and Fiber Glass-Polyester Composite Material. *Int. Res. J. Eng. Technol.* **2016**, *2016*, 1760–1764. Available online: www.irjet.net (accessed on 10 April 2023).
22. Yang, G.; Gao, Z.L.; Xu, F.; Wang, X.G. An Experiment of Fatigue Crack Growth under Different R-Ratio for 2024-T4 Aluminum Alloy. *Appl. Mech. Mater.* **2011**, *66–68*, 1477–1482. [CrossRef]
23. Hudson, M.; Scardina, J. Effect of stress ratio on fatigue crack growth in 7075-T6 Al alloy sheet. *Natl. Symp. Fract. Mech.* **1967**.
24. Wei, R.P. Fatigue-crack propagation in a high-strength. *Int. J. Fract. Mech.* **1968**, *4*, 159–168. [CrossRef]
25. ANSYS. *Meshing Guide*; Finite Elem. Simulations Using ANSYS; Ansys: Canonsburg, PA, USA, 2015; Volume 15317, pp. 407–424. [CrossRef]
26. Araque, O.; Arzola, N. Weld Magnification Factor Approach in Cruciform Joints Considering Post Welding Cooling Medium and Weld Size. *Materials* **2018**, *11*, 81. [CrossRef] [PubMed]
27. Shawe-Taylor, J.; Cristianini, N. *Kernel Methods for Pattern Analysis*; Cambridge University Press: Cambridge, UK, 2004.
28. Demir, S.; Toktamiş, Ö. On the adaptive Nadaraya-Watson kernel regression estimators. *Hacet. J. Math. Stat.* **2010**, *39*, 429–437.
29. Fan, J.; Gijbels, I. *Local Polynomial Modelling and Its Applications*; Applied Pr. New York; CRC Press: Boca Raton, FL, USA, 1996.
30. Chu, C.-Y.; Henderson, D.J.; Parmeter, C.F. On discrete Epanechnikov kernel functions. *Comput. Stat. Data Anal.* **2017**, *116*, 79–105. [CrossRef]
31. Alshoaibi, A.M. Computational Simulation of 3D Fatigue Crack Growth under Mixed-Mode Loading. *Appl. Sci.* **2021**, *11*, 5953. [CrossRef]
32. Rahmatabadi, D.; Pahlavani, M.; Bayati, A.; Hashemi, R.; Marzbanrad, J. Evaluation of fracture toughness and rupture energy absorption capacity of as-rolled LZ71 and LZ91 Mg alloy sheet. *Mater. Res. Express* **2018**, *6*, 036517. [CrossRef]